ACS APPLIED MATERIALS & INTERFACES

www.acsami.org Research Article

# Remote Epitaxy and Phase Diagram of Single-Crystalline Ultrathin $VO_2$ Films on the $TiO_2$(001) Substrate

Zhi Zheng, Xing Li,* Xiang Dong, Tianjun Cai, Yang Wang, Binmin Wu, Ziyu Zhang, Jinshui Miao,* and Yongfeng Mei*

Cite This: ACS Appl. Mater. Interfaces 2025, 17, 70203−70216

Read Online

ACCESS | Metrics & More | Article Recommendations | Supporting Information

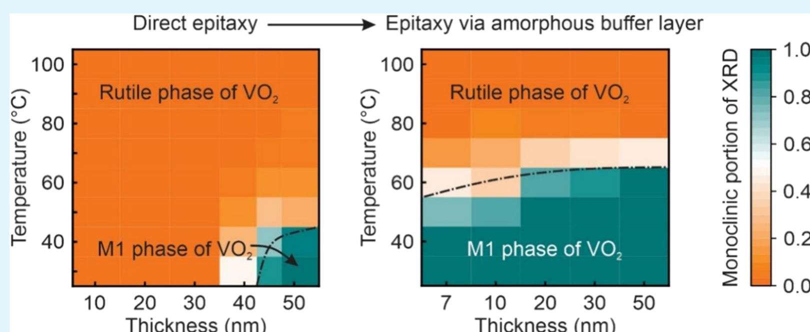


**ABSTRACT:** Ultrathin vanadium dioxide (UT-$VO_2$) films on $TiO_2$(001) provide a model platform to investigate how epitaxial strain, interfacial clamping, and thickness govern structure and the metal−insulator transition (MIT). A quantitative phase-strain-thickness framework is established for single-crystalline $VO_2$ grown by magnetron sputtering, and remote epitaxy—implemented via a nanometer-thin amorphous $Al_2O_3$ interlayer deposited by atomic layer deposition—alleviates interfacial clamping to stabilize the monoclinic M1 phase at room temperature while preserving epitaxial registry. High-resolution characterizations yield a thickness−temperature phase diagram featuring a pinned-rutile regime, a rutile-monoclinic coexistence regime, and a fully relaxed monoclinic regime. Aberration-corrected transmission electron microscopy quantifies the progressive relaxation of the out-of-plane strain across the amorphous interlayer. Combined with first-principles calculations, the results reveal the mechanism of strain-driven phase dynamics and coexistence in UT-$VO_2$, showing that direct epitaxy pins the rutile phase at room temperature and suppresses the resistivity contrast in the ultrathin limit, whereas remote epitaxy reduces residual strain to the subpercent regime, preserves a lowered transition temperature, and substantially amplifies the MIT amplitude without degrading crystallinity. These findings position remote epitaxy as a scalable strain-engineering route for deterministic control of phase and transport in ultrathin correlated-oxide heterostructures.

**KEYWORDS:** *remote epitaxy, phase transition, strain, vanadium dioxide, metal−insulator transition, phase diagram*

Downloaded via FUDAN UNIV on March 9, 2026 at 06:27:08 (UTC).
See https://pubs.acs.org/sharingguidelines for options on how to legitimately share published articles.

## 1. INTRODUCTION

Epitaxy—the growth of a single-crystalline film adopting the lattice structure and orientation of a substrate—is a cornerstone in fabricating high-quality materials for electronics and photonics.[1−4] In complex oxides, it enables precise control over lattice, orbital, and electronic degrees of freedom to access to phenomena like ferroelectricity, magnetism, and phase transitions,[5−7] with a key advantage in lattice mismatch-induced strain, which distorts lattices to modulate material properties, and unlike extreme condition-dependent external pressures/mechanical strains (which often yield metastable phases[8−10]), it stabilizes new structural states, alters electronic band structures, and tailors phase transitions in a controllable manner.[11−18] Remote epitaxy (RE) extends this paradigm by inserting an ultrathin interlayer—classically a single/bilayer graphene—between substrate and film, through which the substrate's long-range electrostatic potential penetrates to preserve lattice registry while the interlayer weakens direct chemical bonding, enabling single-crystal growth with facile, low-damage release and transfer as well as substrate reuse.[19] Recent RE variants use subnanometer amorphous oxides (deposited via atomic layer deposition (ALD)[20]) instead of graphene; these interlayers tolerate high temperatures/oxidizing ambient better, expanding RE to a broader set of oxide thin films. Moreover, RE reshapes strain and defect

Received: September 19, 2025
Revised: December 9, 2025
Accepted: December 9, 2025
Published: December 15, 2025

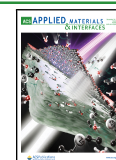


© 2025 American Chemical Society

https://doi.org/10.1021/acsami.5c18705
ACS Appl. Mater. Interfaces 2025, 17, 70203−70216

landscapes in the overlayer, yielding reduced defect densities and lower residual strain relative to direct epitaxy.[21−23]

Vanadium dioxide ($VO_2$), a prototypical correlated oxide, exhibits a sharp, reversible metal−insulator transition (MIT) near 68 °C, switching between a monoclinic semiconducting phase ($P2_1/c$) and a tetragonal metallic phase ($P4_2/mnm$). This transition is accompanied by large changes in the resistivity, optical transmission, and unit cell parameters.[24−29] ultrathin $VO_2$ (UT-$VO_2$) films The functional performance of ultrathin $VO_2$ (UT-$VO_2$) films depends critically on their crystallinity; epitaxial growth minimizes grain boundaries and defects, enhancing transition sharpness and electronic coherence.[20] Importantly, the interfacial strain from the lattice mismatch further tunes the MIT temperature,[30] which is magnified at a reduced thickness. Thus, epitaxial UT-$VO_2$ films provide a versatile platform for studying phase-transition dynamics and engineering phase-change functionalities through strain.

Previous studies have reported elevated properties of single-crystalline UT-$VO_2$ films deposited by various methods, including radio frequency magnetron sputtering (MS), molecular beam epitaxy (MBE), and pulsed laser deposition (PLD).[30−34] UT-$VO_2$ films exhibit a lowered transition temperature, close to room temperature, and even a stable rutile phase at room temperature.[33−35] Moreover, UT-$VO_2$ films also enable applications in the miniaturization of devices while still maintaining high transport properties and sharp MIT processes.[36] In ultrathin epitaxial $VO_2$ on $TiO_2$(001), biaxial epitaxial strain combined with substrate clamping can pin the lattice in rutile symmetry across the insulator−metal transition, producing an isostructural change, whereas thicker films gradually recover into the conventional monoclinic-rutile structural transition.[35,37] However, little attention has been paid to the systematic phase dynamics and crystalline states of UT-$VO_2$ films with various thicknesses or under different strains, and the critical thickness or the strain that $VO_2$ is required to form the room temperature rutile phase is still not clear. The pinned rutile phase in the UT-$VO_2$ regime shows limited MIT properties. In this study, we establish a systematic phase study of magnetron-sputtered UT-$VO_2$ films of various thicknesses to examine the relationship among the thickness of the epilayers, lattice strain, and corresponding crystallographic phases. Moreover, we achieved remote epitaxial UT-$VO_2$ with the help of a nanometer-thin amorphous buffer layer to achieve elevated MIT properties.

## 2. EXPERIMENTAL SECTIONS

**2.1. Density Functional Theory (DFT) Calculations.** All first-principles calculations were performed within density functional theory using the Vienna Ab initio Simulation Package (VASP). Exchange−correlation effects were treated by using the Perdew−Burke−Ernzerhof generalized gradient approximation (GGA-PBE). Core−valence interactions were described using the projector augmented-wave (PAW) method with a plane-wave cutoff of 400 eV. Atomic positions were relaxed until the residual Hellmann−Feynman forces were below 0.01 eV/Å and the total-energy change was less than $10^{-5}$ eV.

**2.2. Thin Film Deposition.** *2.2.1. Deposition of Single-Crystalline $VO_2$.* Single-crystalline $VO_2$ thin films were deposited by using direct current (DC) reactive magnetron sputtering (MS, PVD-75, Kurt J Lesker Company). Before mounting into the MS process chamber, the $TiO_2$(001) substrates (Shanghai Zhongkeshenguang, China) with dimensions of 10 × 10 × 0.5 $mm^3$ were cleaned with acetone, ethanol, and deionized (DI) water for 10 min and a UV ozone cleaner (SC-UV-I, SETCAS LLC, China) for 30 min. A pure 2 in. vanadium source (PrMat, China) was mounted at the DC source position in the chamber. The base working vacuum of the chamber was $5 \times 10^{-5}$ Torr, and the deposition temperature was set to 550 °C. During both the heating and deposition processes, the substrate holder was rotated at 5 rpm to ensure homogeneity. The deposition power was 200 W, and the gas flow rate was 20 sccm Ar and 2 sccm of $O_2$. UT-$VO_2$ films with different thicknesses were grown by adjusting the deposition time. For each 10 nm thickness of UT-$VO_2$, the deposition time was ∼150 s. After $VO_2$ growth, the sample was cooled to room temperature and removed from the chamber.

*2.2.2. Atomic Layer Deposition of Amorphous $Al_2O_3$ Buffer Layer.* For the remote epitaxial samples, the same $TiO_2$(001) substrates were used and cleaned before growth, as described in Section 2.2.1. The interlayer (amorphous $Al_2O_3$) was then deposited by atomic layer deposition (ALD, MNT Micro and Nanotech Co., Ltd., China). The chamber base pressure was 10 Pa, and the temperature was set to 250 °C. For the amorphous $Al_2O_3$ growth, the precursors were trimethylaluminum (TMA, pulse time: 20 ms, purge time: 20 ms) and DI water (pulse time: 20 ms, purge time: 25 ms), with a growth rate of ∼0.11 nm/cycle.

**2.3. Basic Characterizations.** *2.3.1. X-ray Diffraction (XRD).* High-resolution X-ray diffraction (XRD) was performed using a Bruker D8 Advance diffractometer with Cu K$\alpha_1$ radiation ($\lambda$ ∼ 0.15406 nm) and a Ge(004) monochromator. Detailed information about the characteristic crystal plane peaks, out-of-plane lattice spacings, and in-plane epitaxial relationships was obtained by symmetric $2\theta-\omega$ scans and $\phi$ scans. For $2\theta-\omega$ scans, the recording time for each scan step is 0.15 s, and the $2\theta$ angle step is 0.02°. For $\phi$ scans, the recording time for each scan step was 0.15 s, and the $2\theta$ angle step was 0.15°. For reciprocal space mapping (RSM), the slit is 0.2 mm, the scan step is 0.01° for $\omega$ angle, the recording time is 0.1 s, and the offset of $2\theta$ is −1.0°.

*2.3.2. Raman Spectroscopy.* Raman spectroscopy (inVia-Qontor, Renishaw, MA) mapping was performed by focusing on the top surface of the direct and remote epitaxy samples using a 532 nm laser. The acquisition time for each line was 1 s, and an integration of 10 was used to prevent the MIT of the UT-$VO_2$ films during the measurement.

*2.3.3. Electric Transport Property.* The resistance versus temperature plot was conducted with a temperature-controlled stage (CRYOX-MINI, PSAIC, China) and a four-point resistance test system (HPS2663, Helpass Electronic Technologies Inc., China).

*2.3.4. Atomic Force Microscopy.* Thickness measurements were conducted using an atomic force microscope (Bruker Dimension Edge, Bruker) after patterning and etching to create a trench down to the substrate surface for height reference. The working mode was the tapping mode, and the acquisition frequency was 1 Hz.

**2.4. Scanning Transmission Electron Microscopy (STEM) and Atomic Strain Analysis.** *2.4.1. STEM Measurement.* Five cross-sectional samples were fabricated using a focused ion beam (FIB, Helios G4 UX, Thermo Fisher Scientific Inc.) milling with $Ga^+$ ions and mounted on a copper TEM grid for lamella samples. The thinning process for high-resolution observations and imaging was conducted following the standard $Ga^+$ ion thinning process using the same FIB equipment. STEM high-angle annular dark-field (HAADF) imaging was performed to examine the thin film morphology and atomic structure near the interfaces of UT-$VO_2$/$TiO_2$ and UT-$VO_2$/amorphous $Al_2O_3$/$TiO_2$. The sample was characterized by cold field-emission TEM (ARM200F, JEOL, Japan) fitted with an aberration corrector (CS CORRECTOR, CEOS GmbH, Germany) operated at 200 kV. For STEM-HAADF imaging, a semiconvergence angle of 21.4 mrad and a collection angle of 54−220 mrad were used. Scanning nanobeam electron diffraction (NBED) was conducted under the TEM mode of an ARM200F with a spot size of 1, a 150 $\mu$m condenser lens aperture of #1, and a 10 $\mu$m condenser lens aperture of #2.

*2.4.2. Atomic Strain Analysis.* Based on atomic-resolution imaging and drift correction of the interface of UT-$VO_2$/$TiO_2$ and UT-$VO_2$/amorphous $Al_2O_3$/$TiO_2$, the atomic-scale lattice strain was quantified by geometric phase analysis (GPA) performed with Strain$^{+2}$ (v1.8).[38]

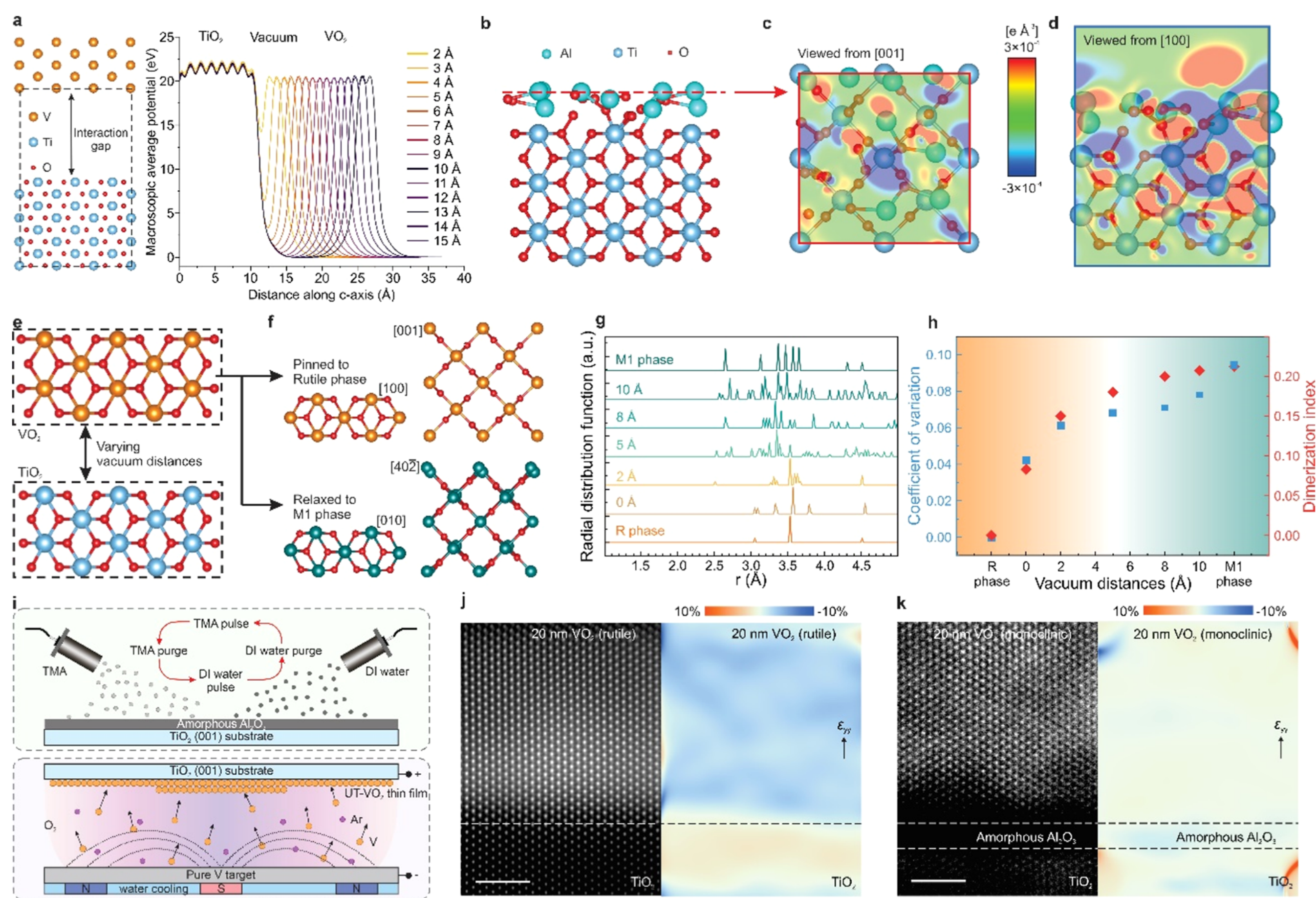


**Figure 1.** Concept and realization of remote epitaxy of ultrathin $VO_2$ (UT-$VO_2$) films on $TiO_2$(001). (a) Schematics and results of DFT calculations of macroscopic average potential along separated slabs of $TiO_2$ and UT-$VO_2$ for remote epitaxy interaction. (b) Atomic structure configuration of amorphous $Al_2O_3$ interlayer on $TiO_2$ substrate in density functional theory (DFT) calculation. (c) Plan-view charge density ($\rho$) contour map of the top surface of the amorphous $Al_2O_3$ interlayer indicated in (b) with a blue line. (d) The cross-sectional $\rho$ distribution contour map. (e) Atomic structure configuration of $VO_2/TiO_2$ heterostructure in lattice relaxation calculation with DFT. (f) V−V bond length statistics in $VO_2/TiO_2$ heterostructures. (g) Radial distribution functions (RDF) of V atoms in remote epitaxy $VO_2/TiO_2$ heterostructures. (h) Phase classification diagram determined by bond length coefficient of variation (CV) and dimerization index ($\eta$). (i) Schematic diagram of the ALD (upper panel) and reactive MS process (lower panel). (j, k) Cross-sectional atomic-resolution STEM-HAADF images of the interface. Right panel in (j) and (k): geometric phase analysis of out-of-plane strain from the STEM images. Scale bars: (j, k), 2 nm.

After subpixel rigid alignment to suppress scan noise, a suitable strain-free region of the $TiO_2$ substrate was chosen as the reference lattice for each measurement. Circular Fourier masks centered on the {110} rutile reflections were applied, followed by phase unwrapping and first-order drift removal. Orthogonal phase gradients supply normal ($\varepsilon_{xy}$, $\varepsilon_{xy}$) and shear ($\varepsilon_{xy}$) components with atomic spatial resolution and high precision. The resulting strain tensors were visualized as red-white-blue color maps directly in the Strain$^{+2}$ software with the corresponding color bar, revealing the tensile and compressive regions across the UT-$VO_2/TiO_2$ and UT-$VO_2$/amorphous $Al_2O_3/TiO_2$ interfaces.

## 3. RESULTS AND DISCUSSION

**3.1. Remote Epitaxy and Strain Alleviation of UT-$VO_2$ on $TiO_2$(001).** To verify the feasibility of remote epitaxy, density functional theory (DFT) computations were performed to probe the transmission of the electric potential from the substrate within the remote configuration as a function of the distance between the substrate and the $VO_2$ epilayer using the Vienna Ab initio Simulation Package (VASP), as shown in Figure 1a. The remote epitaxy system was built with rutile $TiO_2$(001) slabs as the substrate, and a series of vacuum distances between the substrate and epilayer are generated by VASPKIT.[39,40] From the right panel in Figure 1a, an overlap of the planar average electric potential of the substrate and epilayer is present in the interaction gap within a distance of 10 Å and disappears when the gap is increased to more than 10 Å. These findings substantiate the feasibility of our remote epitaxy hypothesis and align with prior computational studies on remote epitaxy in other material systems.[19,20]

Remote epitaxy employing a subnanometer amorphous oxide interlayer has been demonstrated on sapphire substrates.[20] Building on our previous insights into amorphous $Al_2O_3$ interlayers and the fundamental requirement in remote epitaxy that the substrate's periodic potential be only partially transmitted through the buffer layer, we therefore select ALD-grown amorphous $Al_2O_3$ as the interlayer. For the $TiO_2$(001) substrate used here, we first assessed the feasibility by examining the interfacial charge redistribution via DFT charge density difference ($\Delta\rho$) analysis. Specifically, we generated a physically realistic amorphous $Al_2O_3$ interlayer using ab initio molecular dynamics (AIMD), combined it with the $TiO_2$ substrate, and performed full structural relaxation to obtain the heterostructure shown in Figure 1b (the whole process of building and calculating the amorphous structures is shown in



https://doi.org/10.1021/acsami.5c18705
ACS Appl. Mater. Interfaces 2025, 17, 70203−70216

Figure S1). This relaxed model (details in Figure S2) was then used to compute $\Delta\rho$ and evaluate whether remote epitaxy can be realized in the $TiO_2/Al_2O_3$ system. The charge density $\rho$ distribution is then calculated and can be seen on the top surface of amorphous $Al_2O_3$ in Figure 1c. To observe the $\rho$ transferred from the substrate clearly, the cross-sectional $\rho$ distribution is studied along the (100) plane (Figure 1d), which reveals that partial charge can be transferred to the top surface of the amorphous interlayer and its period distribution reveals that the electrostatic potential from the substrate is not completely screened by the amorphous $Al_2O_3$ interlayer.

The crystal structure of remotely epitaxial $VO_2$ on $TiO_2$(001) is crucial to its behavior. At room temperature, sufficiently thin $VO_2$ layers remain pinned in the rutile (R) phase, whereas increasing the thickness or strain relaxation drives a transition toward the monoclinic M1 phase. We also modeled this evolution using DFT calculations to assess whether remote epitaxy effectively modulates the film strain. To emulate the remote epitaxy geometry, we introduced a vacuum spacer (as in Figure 1e) between $TiO_2$ and $VO_2$, relaxed the heterostructures in VASP, and then diagnosed the phase of the relaxed $VO_2$ layer (direct calculation results are shown in Figure S3). Our diagnostics comprise (i) the V−V radial distribution function (RDF) computed from pair-distance statistics, (ii) the coefficient of variation of V−V distances, CV = $\sigma/\mu$, where $\sigma$ is the standard deviation of the V−V distance, $\mu$ is the mean of V−V distances, and (iii) a V-dimerization order index, $\eta = (d_{\mathrm{long}} - d_{\mathrm{short}})/(d_{\mathrm{long}} + d_{\mathrm{short}})$. As shown in Figure 1f, a fully pinned R-phase exhibits eight equivalent V neighbors along the cell-diagonal directions with a uniform separation of ~3.5 Å; viewed along [001], the V atoms form straight, undimerized chains ($\eta \approx 0$, CV $\approx 0$). By contrast, in the relaxed M1 phase the V−V separations split into alternating short (~2.7 Å) and long (~3.1 Å) distances along the out-of-plane direction, yielding a finite $\eta$ and increased CV—clear signatures of Peierls-like dimerization and symmetry lowering from R to M1.[41,42] After the lattice relaxation calculation, the structural results are shown in Figure 1e,f, with different zone-axis views of the rutile and M1 phases of $VO_2$. The radial distribution functions of V atoms are plotted in Figure 1g, and a clear trend of peak splitting around 3.5 Å is shown with increasing vacuum distances, proving that gradual relaxation from pinned rutile to the M1 phase can occur. We classified the remote epitaxy instances using the criteria of CV and $\eta$ in Figure 1h, and the values of the standard R and M1 phases are also plotted for reference.

We align and analyze the crystal structure models of $VO_2$-M1, $VO_2$-R, and $TiO_2$ obtained and verified using open-source databases to visualize their epitaxial relationships.[43,44] For UT-$VO_2$ epitaxially grown on $TiO_2$(001), owing to the well-matched epitaxial relationship, with a zone axis of [100] in rutile $TiO_2$, both the monoclinic (M) and rutile (R) phases of $VO_2$ exhibit clear and strong epitaxial relationships with the substrate. Figure S4 shows the basic schematics of the direct and remote epitaxy samples (both $VO_2$ films are 20 nm thick), proving that remote epitaxial UT-$VO_2$ can relax the top $VO_2$ layer into the monoclinic phase rather than pinning into the rutile phase. According to the lattice correspondence from the atomic models, the high-temperature rutile phase of $VO_2$ matches the crystal system with $TiO_2$, and the $VO_2$-R{011} crystal planes are epitaxially grown from the $TiO_2${011} crystal planes. Monoclinic $VO_2$ will have small torsion and strain in the atomic structure when the strain is present, as the basic crystal system is different from that of the substrate, and the $VO_2$-M{100} crystal planes are epitaxially related to the $TiO_2${011} crystal planes.

The realization of remote epitaxy of UT-$VO_2$ on $TiO_2$(001) substrates with the introduction of a nanometer-thick amorphous $Al_2O_3$ buffer layer is achieved by atomic layer deposition (ALD). The top panel of Figure 1i depicts the process of ALD. During this process, the sequential pulsing and purging of the corresponding precursors produces a uniform ultrathin $Al_2O_3$ layer. In our previous studies, the feasibility of epitaxially growing oxide nanomembranes with the electric field of the substrate penetrating the ultrathin buffer layer was verified.[20] Consequently, the realization of remote epitaxy with the $VO_2/TiO_2$ interface also follows a similar mechanism, where the nanometer-thick amorphous $Al_2O_3$ buffer layer only screens the partial electric field from the substrate. ALD-buffered and pristine $TiO_2$(001) substrates are then transferred to reactive magnetron sputtering of UT-$VO_2$ films of various thicknesses, as shown in the bottom panel of Figure 1i. Because the lattice of the epilayer is not completely bonded with the lattice of the substrate in the remote epitaxy configuration, the residual strain is further relaxed and is no longer completely pinned to the rutile phase at room temperature. In Figure S4, the lattice schematics of the direct and remote epitaxy samples are illustrated, showing the epitaxial strain in UT-$VO_2$, where the in-plane strain induced by lattice mismatch leads to the pinning of rutile UT-$VO_2$.[30,33] The growth direction of direct epitaxy UT-$VO_2$ is $VO_2$ R[001] and $VO_2$ M[$40\bar{2}$] for the remote epitaxy samples. In Figure S4a, the cube depicted by the dotted line represents a vanadium dioxide thin film crystal in the unstrained state. The smaller dimensions in the in-plane direction and larger ones in the out-of-plane direction compared with the light orange cube indicate the tensile strain in the *xy*-plane and compressive strain in the out-of-plane direction.

A key difference between the direct and remote epitaxy samples lies in the strain field across the epitaxy interface. To visualize and measure the precise atomic-level epitaxial strain in the samples, two cross-sectional lamellar TEM samples are prepared following the steps described in Section 2.3.1 for the 20 nm thick $VO_2$ direct and remote epitaxy samples. In the left panels of Figure 1j,k, both direct and remote epitaxial relationships are clearly observed in the cross-sectional atomic images of the two samples. The ultrathin $Al_2O_3$ buffer layer in Figure 1k appears dark with low contrast because of the mechanism of interactions with electrons of amorphous materials and the lack of electron channeling effect in STEM imaging.[45,46] The coverage of the buffer layer is continuous across the entire film, as discussed in later sections. The right panels in Figure 1j,k show the GPA mapping results for the out-of-plane epitaxial lattice strain ($\varepsilon_{yy}$). Some turbulence and fluctuations in the measured results at the edge of the image are due to periodic boundary conditions and artifacts in the real-space image. The main part of the GPA results shows significant differences between the direct and remote epitaxial UT-$VO_2$ in terms of the out-of-plane strain. The presence of the buffer layer partially relieves epitaxial strain in the system, even at the earliest stages of film growth, thereby promoting lattice relaxation and offering substantial freedom for strain modulation. This, in turn, enables a more in-depth investigation of the epitaxial strain, phase dynamics, and correlations with the metal−insulator-transition properties of UT-$VO_2$.


https://doi.org/10.1021/acsami.5c18705
ACS Appl. Mater. Interfaces 2025, 17, 70203−70216

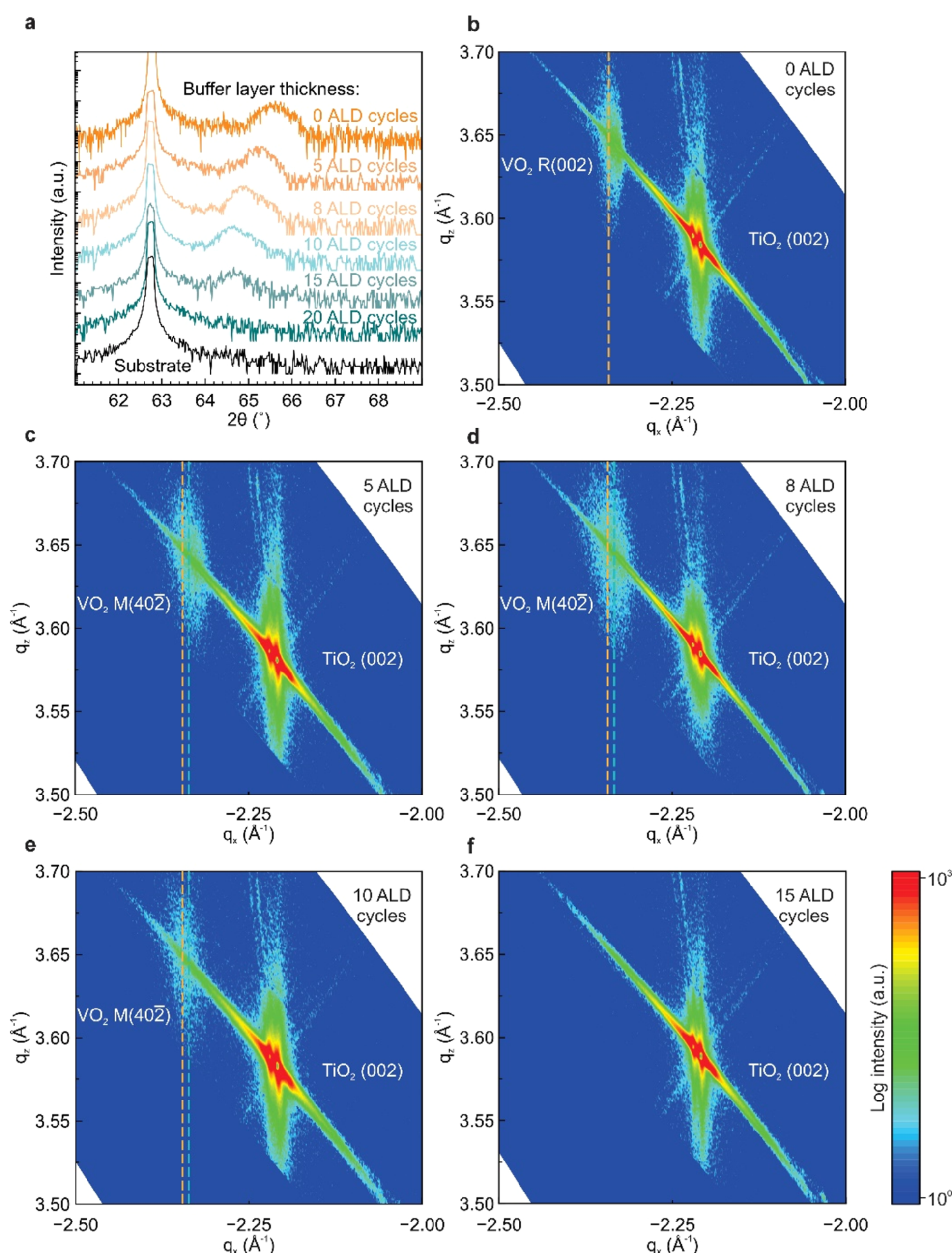


**Figure 2.** Crystallographic characterization of remote epitaxy of UT-$VO_2$ films on $TiO_2$(001). (a) XRD plots of 20 nm thick UT-$VO_2$ with different cycles of buffer layer on $TiO_2$(001). (b–f) Reciprocal space mapping (RSM) around the $TiO_2$(002) peak. The dashed orange and teal lines indicate the $q_x$ coordinates of the $VO_2$ rutile (002) and $VO_2$ monoclinic ($40\bar{2}$) peaks, respectively.

We conduct high-resolution XRD $2\theta$ scans, $\phi$ scans, and reciprocal space mapping (RSM) to study the crystallographic phases of 20 nm thick UT-$VO_2$ under different epitaxial conditions. Figure 2a shows the XRD $2\theta$ scan plots of the samples. The XRD pattern shows a sharp peak at approximately 62.7°, which corresponds to the (002) peak of the $TiO_2$ substrate. Owing to the absence of other peaks detected in the XRD signals from the first five samples, all $VO_2$ films are highly oriented and have a pure phase. As the thickness of the amorphous buffer layer increases, the peak intensity of $VO_2$ decreases and the characteristic peaks of $VO_2$ increase from 64.9 to 65.7° as a function of the buffer layer thickness (zoomed XRD plots and photos are shown in Figure S5). According to the standard crystal models, the (001) plane of rutile $VO_2$ (Crystallography Open Database Card 1548819) has a lattice spacing of 2.8528 Å, which corresponds to a $2\theta$ value of 65.4° for the (002) plane. For the monoclinic phase $VO_2$ (Crystallography Open Database Card No. 9009089), the most matched lattice plane is the ($40\bar{2}$) plane, with a lattice spacing of 2.8715 Å and a corresponding $2\theta$ angle of 64.9°. The calculated values of the $2\theta$ peak positions of the rutile and monoclinic $VO_2$ phases match well with the measured XRD patterns. The shifting of the characteristic peak indicates a phase transition from a conventional pinned-rutile phase at room temperature toward the monoclinic phase with the help of a buffer layer.[30,33,35] The $VO_2$ (002) or ($40\bar{2}$) reflection vanishes after 20 ALD cycles because an excessively thick amorphous $Al_2O_3$ interlayer suppresses the substrate's periodic potential and destroys the epitaxial template mechanism, leading to nearly polycrystalline $VO_2$ with randomly oriented


https://doi.org/10.1021/acsami.5c18705
ACS Appl. Mater. Interfaces 2025, 17, 70203−70216

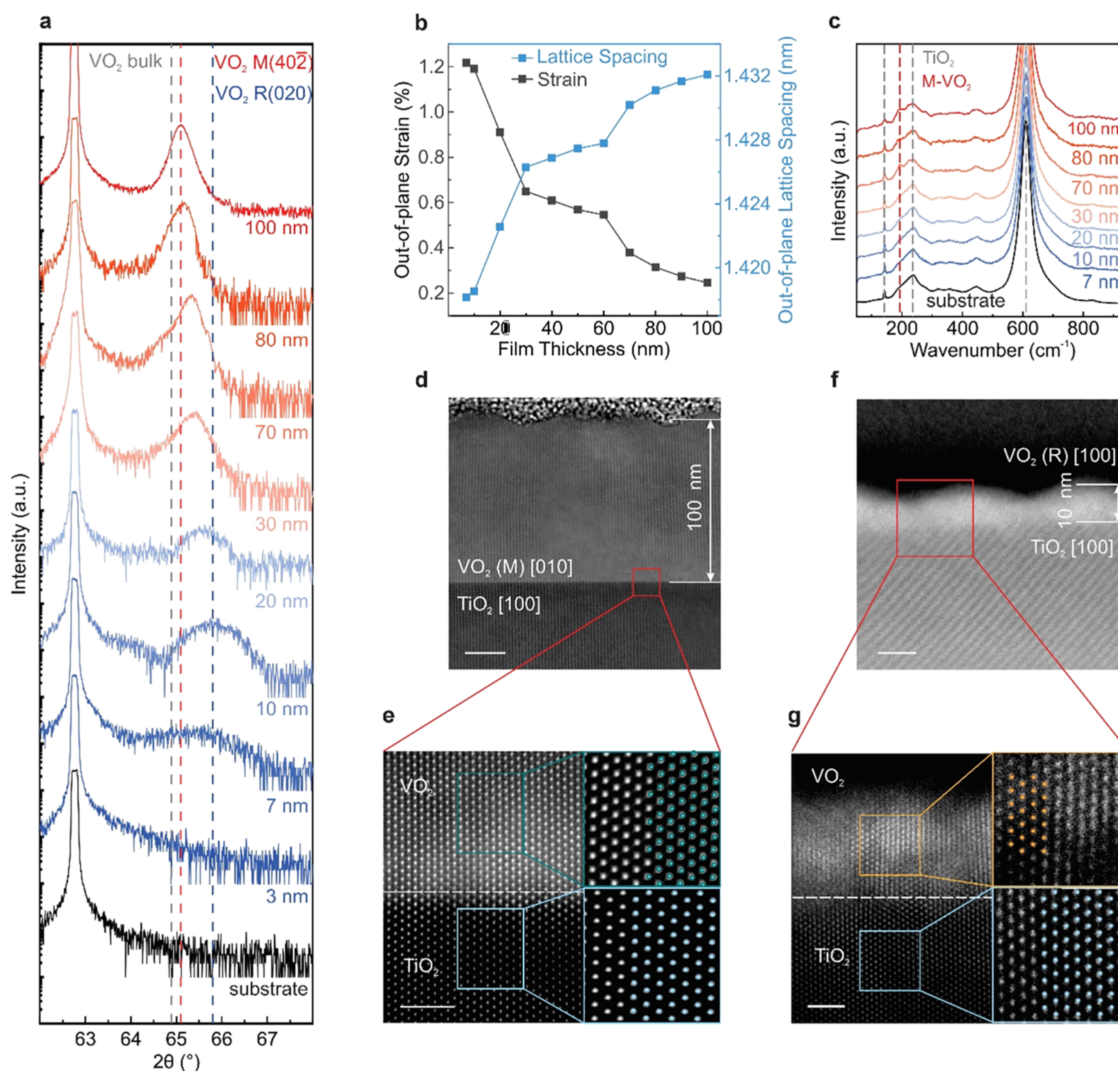


**Figure 3.** Crystallographic characterization of remote epitaxy of UT-$VO_2$ films on $TiO_2$(001). (a) XRD $2\theta$ plots of UT-$VO_2$ of different thicknesses on $TiO_2$(001). (b) Out-of-plane strain and lattice spacing plots of direct epitaxy samples with different thicknesses. (c) Raman spectroscopy plot of epitaxy samples. (d) Cross-sectional STEM-HAADF image of the 100 nm thick epitaxy sample. (e) Atomic-resolution STEM-HAADF image of the interface in (d). (f) Cross-sectional STEM-HAADF image of the 10 nm thick epitaxy sample. (g) Atomic-resolution STEM-HAADF image of the interface in (f). Scale bars: (d) 20 nm, (e) 3 nm, (f) 5 nm, and (g) 3 nm.

grains whose Bragg peaks are redistributed to other lattice planes outside the measured $2\theta$ window.

Figure 2b−f shows the results of the high-resolution RSM of UT-$VO_2$ on $TiO_2$(001) with a series of buffer layer thicknesses. In RSM, the horizontal and vertical axes represent the in-plane and out-of-plane components of the scattering vector, respectively. The highest-intensity feature corresponds to the $TiO_2$ substrate (002) reflection, and the out-of-plane reflections of the $VO_2$ overlayer are likewise observed for all of the remote epitaxy samples. As shown in Figure 2b−f, the characteristic $VO_2$ peak diminishes with an increasing interlayer thickness and eventually vanishes. The peak position also evolves: in Figure 2b the $VO_2$ peak coincides with the rutile (R)-phase (002) reflection (orange dashed line), whereas in Figure 2c−e it progressively shifts to the monoclinic M1-phase ($40\bar{2}$) reflection (blue dashed line).

**3.2. Pinning Effects and Thickness−Strain Relationships of UT-$VO_2$.** Previous studies have reported the formation of both monoclinic and rutile ultrathin $VO_2$ films on $TiO_2$ by radio frequency magnetron sputtering, molecular beam epitaxy, and pulsed laser deposition.[30,31,33] Viewed from the [100] zone axis of the $TiO_2$ substrates, the monoclinic phase $VO_2$ shows the [010] zone axis, and the growth direction is [$40\bar{2}$]. Rutile $VO_2$ exhibits a [100] zone axis and a [001] growth direction, which matches the $TiO_2$ substrates. In this regime, the structural phase transition introduces a slight crystal cell distortion and changes in the unit cell volume and symmetries.

We examined UT-$VO_2$ films of different thicknesses by parallel incident beam XRD measurements, and the results are shown in Figure 3a. Upon increasing the thickness, the $VO_2$ diffraction peak shows a clear shift to lower angles (shown by the guided line). In the pattern of the 100 nm thick film, the $VO_2$ diffraction peak shifts to $2\theta = 64.9°$, which is consistent with the ($40\bar{2}$) diffraction of pure M1-$VO_2$ compound (JCPDS card No. 82-0661). The ultrathin $VO_2$ film shows a larger diffraction angle close to the (002) diffraction peak of rutile $VO_2$ (JCPDS card No. 79-1655), which is associated with interfacial strain. Considering the lattice parameters of the standard rutile $TiO_2$ ($a = b = 0.458$ nm) and tetragonal $VO_2$ ($a$


https://doi.org/10.1021/acsami.5c18705
ACS Appl. Mater. Interfaces 2025, 17, 70203−70216

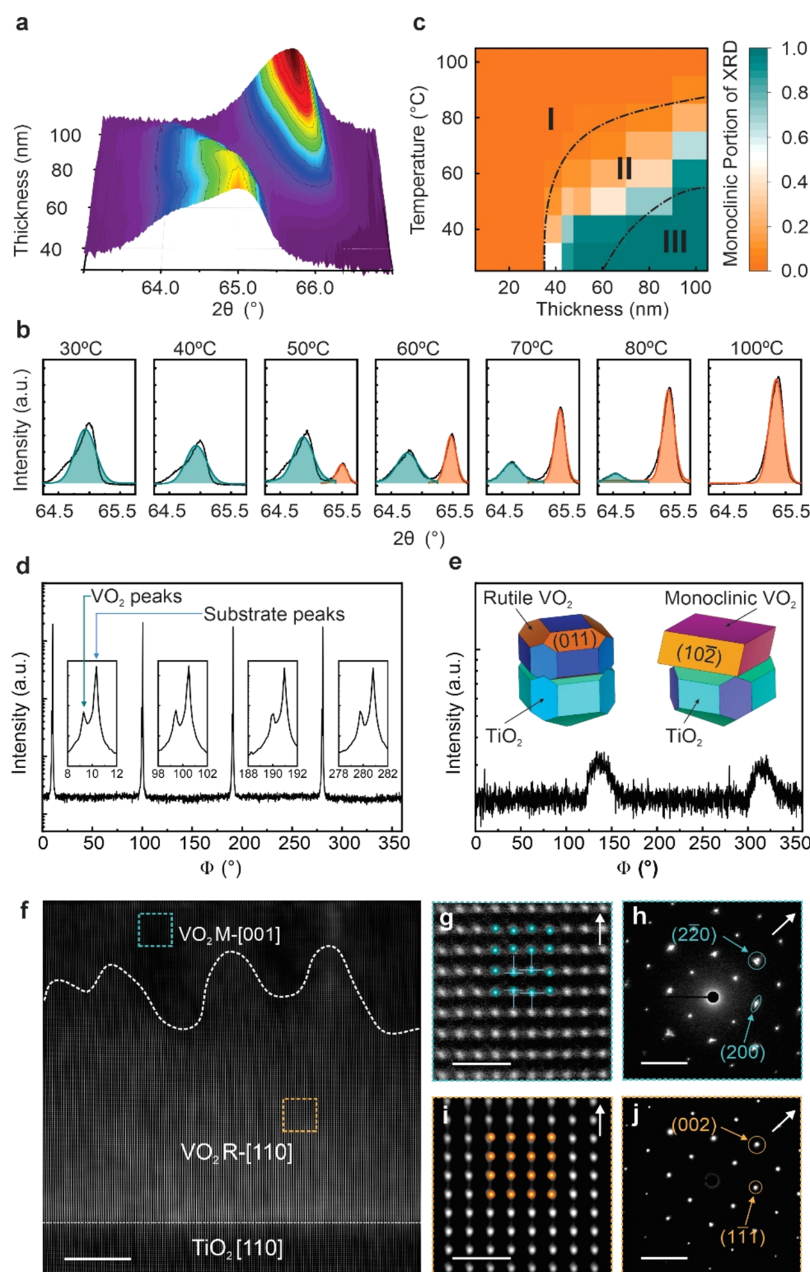


**Figure 4.** Phase transition and coexistence of UT-$VO_2$ films on $TiO_2(001)$. (a) In situ XRD plots of 80 nm thick UT-$VO_2$. (b) Representative XRD peaks at several temperatures during the in situ heating scans, fitted with two Gaussian peaks corresponding to the monoclinic (~64.9°, dark teal) and rutile (~65.4°, orange) phases. (c) Phase diagram of $VO_2$ of different thicknesses and temperatures. The color bar shows the monoclinic portion of the XRD peaks extracted from data described in (b), and the phase diagram is divided into three zones according to the monoclinic portion of $VO_2$. Zone I: all rutile phases. Zone II: mixed monoclinic and rutile phase. Zone III: all monoclinic phases (full XRD data in Figure S6). (d) $\phi$ scans of the (011) crystal planes of the rutile phase and (e) $\phi$ scans of $(10\bar{2})$ crystal planes of the monoclinic phase. (f) Atomic-resolution STEM-HAADF images of the cross-section of the 50 nm thick $VO_2$ thin film on $TiO_2$ substrate. (g, i) Magnified atomic image of the corresponding areas indicated by cyan and orange dashed rectangles. (h, j) NBED patterns acquired at the corresponding areas where (g) and (i) are taken. Scale bars: (f) 20 nm, (g, i) 5 nm, (h, j) 5 $nm^{-1}$.

= $b$ = 0.455 nm), the initial $VO_2$ film layer grows epitaxially on the $TiO_2(001)$ surface following the tetragonal lattice structure in the growth plane (Figure 1b). In this initial stage, a large strain occurs in the ultrathin $VO_2$ film. The gray dashed lines indicate the characteristic peaks of the $TiO_2$ substrate, while the red dashed line is the reference peak position for monoclinic $VO_2$. Owing to its metallic nature, no characteristic peak is observed present.[47,48] With the help of aberration-corrected STEM (Figures 1j,k and 3e,g), the epitaxial relationship is confirmed. Moreover, the epitaxial orientation relationships between the film and substrate are $(001)VO_2//(001)TiO_2$ and $[100]VO_2//[100]TiO_2$. The shifting of peak positions among the samples with different thicknesses is similar to that of the remote epitaxy samples, indicating that the thickness plays a role similar to that of the buffer layer in terms of strain or lattice relaxation. Figure 1b shows the out-of-plane lattice spacing of $VO_2$, extracted from the XRD reflections, together with the corresponding out-of-plane strain ($\varepsilon_\perp$). Owing to the epitaxial growth of the UT-$VO_2$ films, the strong characteristic peaks in the XRD $2\theta$ scans arise from the


https://doi.org/10.1021/acsami.5c18705
ACS Appl. Mater. Interfaces 2025, 17, 70203−70216

major crystal planes parallel to the substrate (plane vector normal to the substrate). When grown on $TiO_2(001)$, ultrathin $VO_2$ is under out-of-plane compression; for the thinnest film (~3 nm), $\varepsilon_\perp \approx 1.2\%$. With increasing thickness, the strain progressively relaxes, and the average lattice mismatch decreases. For 30−70 nm thick $VO_2$, the out-of-plane strain decreases moderately, while for UT-$VO_2$ films thicker than 70 nm, the out-of-plane strain continues to decrease as the thickness increases. However, during 60−80 nm, the strain relaxation becomes further accentuated, giving rise to a local maximum of the slope within this range. The progress of the strain alleviation in the UT-$VO_2$ of different thicknesses is not only due to the layer-by-layer lattice relaxation in the epitaxy system but is also highly related to the crystallographic or phase composition of the film,[17] which is being focused on in the later part of this study. Figure 3c shows the Raman spectra versus thickness. Phase identification is based on V−V vibrational modes: monoclinic M1 $VO_2$ exhibits a strong feature near ~192 $cm^{-1}$. This peak disappears when the thickness falls below ~30 nm, indicating a transition to the rutile (R) phase in the ultrathin limit, as the rutile/metallic phase of $VO_2$ emerges with electron screening effect of the Raman scattering, which is consistent with the XRD-derived strain evolution.

To compare the fully relaxed monoclinic and the pinned rutile film, two lamella samples are prepared by focused ion beam milling, as described in Section 2.3.1, and we observe the atomic configurations of the samples with aberration-corrected scanning transmission electron microscopy (STEM) and low-magnification high-angle annular dark-field (HAADF) cross-sectional images, as shown in Figure 3d,f. In the HAADF images, the zone axes toward the $TiO_2$ substrates are both aligned in the [100] orientation, while the relaxed and pinned epilayers are different in crystallographic phases; their zone axes are M [010] and R [100], respectively. The thickness of the relaxed monoclinic sample is 100 nm, and that of the pinned rutile sample is 10 nm. UT-$VO_2$ shows a clear and flat interface with the $TiO_2$ substrate, and no crystal border or grain border is visible due to the highly matched lattice configuration and thus the single-crystal configuration. For the 100 nm thick UT-$VO_2$, the epilayer relaxes to a pure monoclinic phase. The blue and teal rectangles are zoomed-in areas for atomic observations of $VO_2$ and the substrate, respectively, as shown in Figure 3e. In Figure 3d,e, UT-$VO_2$ shows a pure monoclinic configuration, where the atomic models of V atoms represented by dark teal circles precisely match the atoms in the image. Figure 3g shows the atomic-resolution STEM image of the $VO_2$−$TiO_2$ interface, which shows a clear and flat interface, indicating that the DC magnetron sputtering of $VO_2$ does not damage the surface of the substrate. The upper part of the image has a brighter contrast than the lower part, which is due to the scattered electron dose in the HAADF configuration. V atoms are heavier than Ti atoms; thus, in HAADF-STEM, according to the contrast-formation mechanism, the V-rich region would show a higher contrast.[49−51]

### 3.3. Phase Coexistence and Segregation of Monoclinic and Rutile Phases in UT-$VO_2$.

We conduct in situ heating XRD measurements to further investigate the crystallographic states of ultrathin $VO_2$. Figure 4a shows the characteristic peaks of epitaxial $VO_2$ in situ XRD $2\theta$ scans of the 80 nm-thick $VO_2$ on $TiO_2(001)$ substrate, measured upon heating from 30 to 100 °C, with a 10 °C step. As the temperature increases, the monoclinic peak starts to decrease in height, and the monoclinic peak completely disappears at approximately 90 °C. Meanwhile, the characteristic peak of the rutile phase arises when the temperature reaches above 60 °C. We apply in situ measurements to UT-$VO_2$ films from 7 to 100 nm thickness to systematically study the relationship between the thickness, strain, and crystallographic phases. As Figure 4b illustrates, for each $2\theta$ scan during the heating process of each sample, the monoclinic and rutile peaks are extracted and measured in intensities for further analysis of the monoclinic portion from the XRD signal. All the quantitative analyses of the monoclinic portion of the XRD signals are plotted in the phase diagram, as illustrated in Figure 4c, where the $x$- and $y$-axes are the thickness and temperature, respectively, and the color map shows the monoclinic portion where the orange area indicates the pure rutile phase and the dark teal area indicates the pure monoclinic phase. From the phase diagram, two clear borders can be observed, dividing the phase diagram into three zones. Zone I is the pure rutile phase, zone II is the phase coexistence regime, and zone III is the pure monoclinic phase.

The distribution of the different phases significantly influences the properties of the thin film when mixed phases are present. Previous studies have exhibited a grain-like phase coexistence in thin films of phase-change materials.[52] Figure 4d,e show the $\phi$ scan results of the 40 nm-thick crystal planes (011) in rutile phase $VO_2$ and $(10\bar{2})$ in monoclinic phase $VO_2$, where the schematics of crystal models of UT-$VO_2$ films on $TiO_2(001)$ substrates are shown as insets in Figure 4e, with the crystal planes being measured as indicated by the plane index and their corresponding colors. From the $\phi$ scans, both plots exhibit periodic signals that match the symmetry of the crystal plane itself, indicating evidence of the epitaxial relationship of both the monoclinic and rutile phases of $VO_2$ with the $TiO_2$ substrates, thus facilitating the coexistence of the two crystallographic phases of the UT-$VO_2$ films in zone II from the phase diagram established in this study. The broad $\phi$-scan peaks in Figure 4e originate from a strong depth-dependent mosaic twist induced by the vertical strain gradient and R/M1 phase coexistence in the 40 nm $VO_2$ film, where the relaxation from a fully coherent rutile interface to a partially relaxed monoclinic surface generates a high density of planes with slight disorientation.

To investigate the microscopic distribution of the phase coexistence of the monoclinic and rutile phases in UT-$VO_2$ with proper thicknesses, we make a cross-sectional sample of the 40 nm thick $VO_2$−$TiO_2$ sample by focused ion beam (FIB) milling. An overview of the cross-section of the interface of $VO_2$ and $TiO_2$ is presented in Figure 4g, with the zone axis of $TiO_2$ being [110]. Figure 4g,i shows atomic-resolution HAADF-STEM images of the monoclinic $VO_2$ and rutile $VO_2$ portions, respectively. In agreement with the XRD results, the two phases are confirmed by atomic-level crystallographic characterizations, and the interface is indicated by the white dashed line. The inset in Figure 4g shows the atomic model of monoclinic $VO_2$ viewed from the [001] zone axis, where each V atom slightly deviates from the standard tetragonal positions, resulting in the dimerization of certain V atoms. Figure 4h,j shows the nanobeam electron diffraction (NBED) patterns taken at the corresponding locations of the sample. The deviation of the atom positions from tetragonal symmetry to monoclinic symmetry can be viewed in the NBED patterns with more clarity. In Figure 4h, the spots corresponding to the $(02\bar{2})$ and (200) planes of monoclinic $VO_2$ show broadening

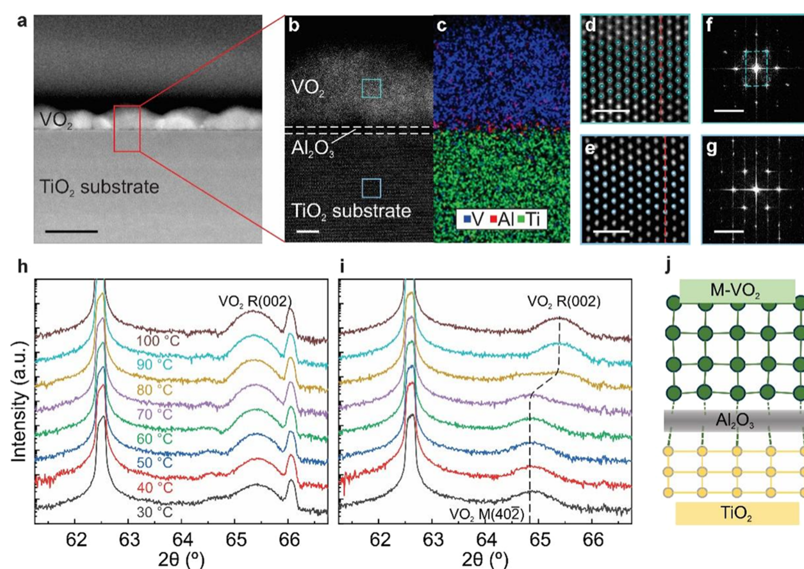


**Figure 5.** Crystallographic characterization of remote epitaxy UT-$VO_2$ films on $TiO_2$(001). (a) Cross-sectional STEM-HAADF image of the remote epitaxial UT-$VO_2$ film with 10 cycles of ALD $Al_2O_3$. (b) Zoomed-in cross-sectional STEM-HAADF image of the zoomed-in area in (a). (c) EDX mapping of the interface of the remote epitaxy sample. (d, e) Atomic-resolution images of the epilayer and substrate in (b). (f, g) Corresponding FFT patterns from the cyan and yellow dashed rectangle in (d) and (e). (h, i) In situ XRD scans of 20 nm UT-$VO_2$ without and with $Al_2O_3$ buffer layer. The positions of the $VO_2$ peaks are indicated with black dashed lines. (j) Atomic model in the remote epitaxy system, where the UT-$VO_2$ films are fully relaxed into the M1 phase. Scale bars: (a) 20 nm, (b) 3 nm, (d, e) 1 nm, and (f, g) 5 $nm^{-1}$.

and distortion effects, making them no longer discrete spots but shapes with finite areas. In the pure rutile $VO_2$ portions, the NBED pattern shows obvious discrete spots on the lattice planes. To differentiate the effect of the phase transition from epitaxial strain, which could also affect the positions of atoms, NBED is also conducted at the interface of $VO_2$ and $TiO_2$. From the NBED of the interface, certain spots move along the direction that is parallel to the interface, which is a characteristic feature of epitaxial strain, as it causes the lattice to be under compressive or tensile stress and strain along the same direction. Therefore, the deviations of the diffraction spots from the standard tetragonal symmetry in Figure 4h with broadening and distortions (different from the peak splitting shown in Figure S8) are evidence of the presence of the monoclinic phase $VO_2$.

**3.4. Microscopic Mechanism of Pinning Relaxation in Remote Epitaxial UT-$VO_2$.** To reveal the microscopic nature of the remote epitaxial UT-$VO_2$ films, the 10 nm $VO_2$−$Al_2O_3$−$TiO_2$ sample is also cut with FIB, and we observe the cross-section of the sample with aberration-corrected STEM. From Figure 5a−c, the amorphous buffer layer can be clearly observed (dark tile between the $TiO_2$ substrate and $VO_2$). Because ALD $Al_2O_3$ is amorphous, there are no periodic graphical patterns in the interlayer. From Figure 5c, energy-dispersive X-ray spectroscopy (EDX) clearly maps the existence of Al. Figure 5d,e shows the atomic-resolution HAADF-STEM image of the sample, and Figure 6f,g shows the fast Fourier transform (FFT) of the zoomed-in images in the corresponding locations. In Figure 5d, the zone axis is [010] of the M1 phase of $VO_2$, and the atoms are aligned with the M1 phase of the unit cell model. The zone axis of the substrate in Figure 5e is [100]. The two FFT patterns (Figure 5f,g) show different patterns of the reciprocal lattice, indicating that the crystal systems of the $VO_2$ and $TiO_2$ substrates are different. The strongest spots in Figure 5f are indicated by the cyan dashed parallelogram, and there is a small tilt (~2°). In situ XRD experiments are also conducted to reveal the structural information on the remote epitaxial UT-$VO_2$ films. Figure 5h,i shows the in situ XRD from 30 to 100 °C of 20 nm UT-$VO_2$ film without the $Al_2O_3$ buffer layer (left) and with $Al_2O_3$ buffer layer (right). The changes in the peak positions clearly show the transition of the $VO_2$ crystal structure from the monoclinic phase (characteristic peak at 64.9°) to the rutile phase (characteristic peak at 65.4°) with increasing temperature. The features around 66.1° come from the polyimide sample holder designed for heating experiments (details in Figure S7). Based on the experimental results, Figure 5j shows the atomic models of the remote epitaxial UT-$VO_2$ films, as the top layer $VO_2$ is fully relaxed to the monoclinic phase.

**3.5. Enhanced MIT Properties of Remote Epitaxial UT-$VO_2$.** To connect the crystallographic and strain states with the transition properties of the UT-$VO_2$ films, we conduct electrical transport property measurements upon heating and cooling of the UT-$VO_2$ films. Figure 6a shows the resistivity with respect to the temperature of the UT-$VO_2$ films on $TiO_2$(001) substrates measured upon heating and cooling. For thicker UT-$VO_2$ films, the resistivity changes during MIT exceed 4 orders of magnitude, indicating a high quality of deposition. With thinner thickness, the resistivity changes during the MIT of $VO_2$ on $TiO_2$ substrates decrease from ~45,000 to <1000 with a thickness of ~7 nm. As the thickness decreases, phase coexistence starts to emerge, and more portions of the UT-$VO_2$ films turn into the rutile phase, thus limiting the MIT performance. Figure 6b plots the MIT temperature of UT-$VO_2$ films, where the transition temperature of thin films on $TiO_2$(001) substrates shows a clear decreasing trend with decreasing thickness or increasing lattice strain. The low transition temperatures of the UT-$VO_2$ samples are also signs of the pinning effect and the presence of the room temperature rutile phase.

We then plot the transition temperatures of the UT-$VO_2$ films from the electrical transport measurements, the out-of-


https://doi.org/10.1021/acsami.5c18705
ACS Appl. Mater. Interfaces 2025, 17, 70203−70216

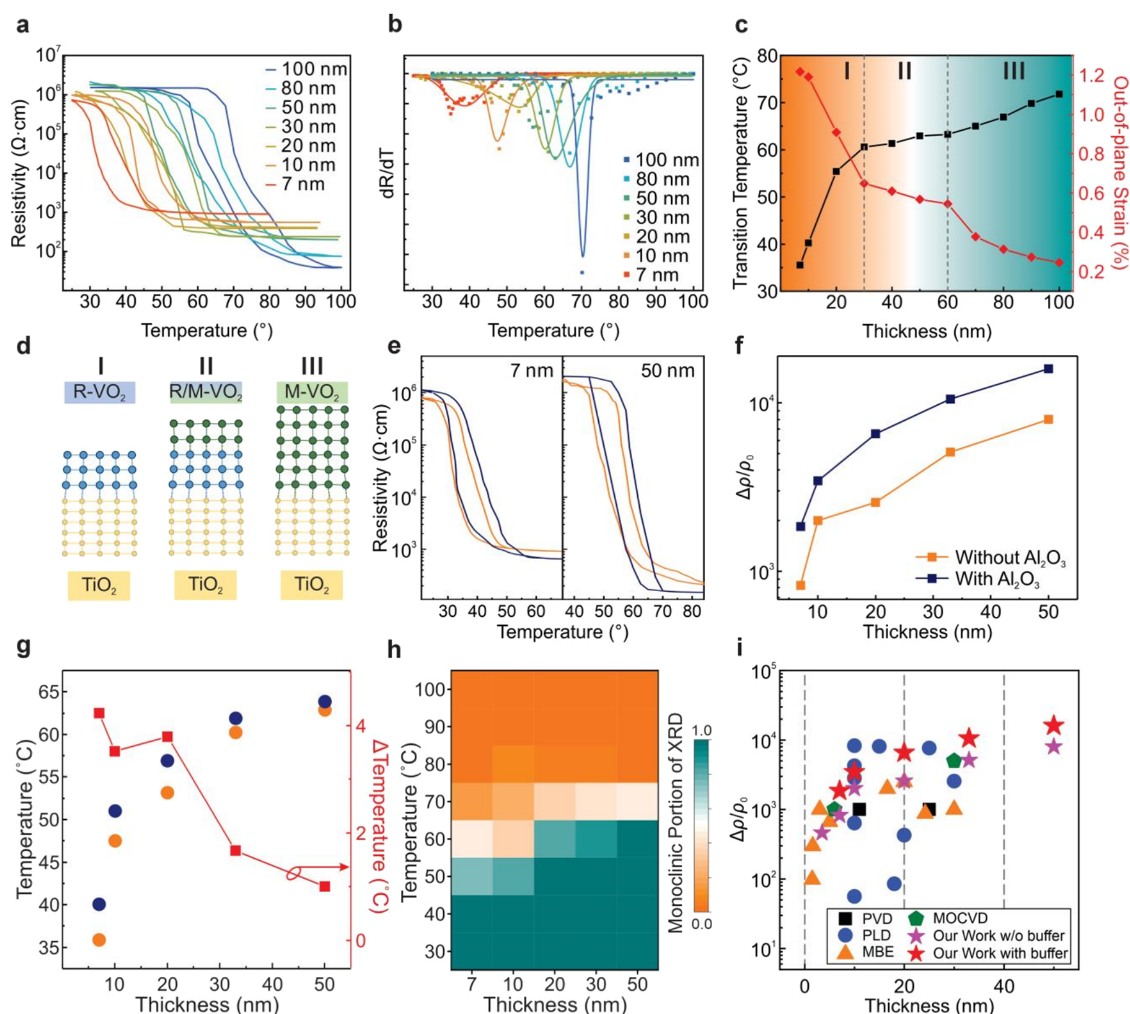


**Figure 6.** Transport property enhancements of UT-$VO_2$ on $TiO_2$(001) via remote epitaxy. (a) The resistivity−temperature curves of UT-$VO_2$ films of different thicknesses. (b) Transition temperatures plotted by the derivative of resistivities of $VO_2$ on $TiO_2$ substrates of various thicknesses, measured upon heating. (c) Transition temperatures and out-of-plane strain of UT-$VO_2$ films with various thicknesses. The color shading shows the corresponding crystallographic phases according to the XRD scans in this study. (d) Lattice model of $VO_2$ on $TiO_2$ substrates. From left to right: all rutile phases, monoclinic and rutile phase coexistence, and all monoclinic phases. (e) The resistivity−temperature curves of RE-UT-$VO_2$ films of different thicknesses. (f) Changes in resistivity before and after the MIT of RE and direct epitaxial UT-$VO_2$ on $TiO_2$(001) (full data in Figure S9). (g) Critical MIT temperature of RE and direct epitaxial UT-$VO_2$ on $TiO_2$(001), labeled by blue and orange squares, and the differences of MIT temperatures between the RE and direct epitaxial samples at the same thickness, labeled by the red squares and line. (h) Phase diagram of RE-UT-$VO_2$ of different thicknesses and temperatures. (i) Benchmark of changes in resistivity before and after the MIT of RE and direct epitaxy UT-$VO_2$, data are taken from refs 30−34,53−59.

plane strain from the XRD scans with the thickness, and the phase diagram of the UT-$VO_2$ films, as shown in Figure 6c. The color-shaded areas represent the three crystallographic zones that describe the states of the UT-$VO_2$ films. From left to right are the pure tetragonal zone (I), mixed phase zone (II), and pure monoclinic phase zone (III). The transition temperatures of the UT-$VO_2$ films show clear characteristics of the crystallographic phases and zones in the phase diagram. For UT-$VO_2$ films in zone I, the transition temperatures are largely affected by the lattice strain and decrease drastically to 35 °C with increasing strain. However, in zones II and III, the transition temperature gradually increases as the strain relaxes. For zone III UT-$VO_2$ films, the transition temperature almost reaches the value of the bulk material (∼68−70 °C). Figure 6d shows the phase dynamics model with the $VO_2$ and $TiO_2$ lattices. For the UT-$VO_2$ films in zone I, the lattice epitaxial strain is large, and the thickness is too small for valid lattice relaxation; thus, the entire crystal lattice is pinned to the rutile phase even at relatively low temperatures (just above room temperature). For UT-$VO_2$ films in zone III, the lattice strain is largely or even fully relaxed because of the sufficiently thick epilayer; thus, the entire lattice is relaxed to the monoclinic phase when the temperature drops below the MIT. However, in zone II, the thickness of the $VO_2$ epilayer is between the critical point of pure rutile and pure monoclinic phases; therefore, the epilayer consists of two phases at room temperature, which also induces the fact that zone II UT-$VO_2$ films exhibit medium electrical transport properties compared with samples from zones I and III.

The pinning effect from the epitaxial relationship with $VO_2$ and $TiO_2$ is the main reason for the limitations in phase transitions, especially in preventing rapid and considerable changes in resistivity. As described earlier, we apply the concept of remote epitaxy after validating it with DFT calculations, where a buffer layer is introduced on top of the $TiO_2$ substrate, enabling the alleviation of the epitaxial strain at


https://doi.org/10.1021/acsami.5c18705
ACS Appl. Mater. Interfaces 2025, 17, 70203−70216

the interface.[20,23,60,61] We deposit an amorphous $Al_2O_3$ buffer layer on top of the substrate before MS deposition and compare the MIT properties of the remote epitaxy samples with those of the original direct epitaxy samples.

Building on the calculations and measurements in Figures 1 and 2, we first chose an interlayer thickness of 10 ALD cycles as a robust condition, then deposited a series of ultrathin $VO_2$ (UT-$VO_2$) films with varying thicknesses and benchmarked their metal−insulator transition (MIT) against direct epitaxial control of the same thickness (Figure 6e). The five panels in Figure 6e (left to right) correspond to $VO_2$ values of 7, 10, 20, 33, and 50 nm, respectively. The remotely epitaxial films exhibit a markedly higher room temperature resistivity than their direct-epitaxy counterparts, with the disparity becoming more pronounced at smaller thicknesses. In addition, the MIT hysteresis in the remote epitaxy samples shows no appreciable broadening, which is an advantage for fast, high-response electronic devices. From these $R-T$ curves, we extracted the resistance change across the transition (e.g., $R_{off}/R_{on}$) and transition temperature, as summarized in Figure 6f,g. Notably, the remote epitaxy films deliver a clear improvement in MIT performance (for 20 nm $VO_2$, an increase of ∼160% in resistance change) without a significant increase in the transition temperature relative to direct epitaxy. Thus, single-crystal UT-$VO_2$ grown by remote epitaxy achieves both an enhanced switching contrast and a comparatively low $T_{MIT}$, which is desirable for energy-efficient electronics. Because RE relaxes interfacial strain, RE-UT-$VO_2$ is no longer pinned in the rutile state at room temperature. Consistent with this picture, the thickness-dependent phase diagram in Figure 6h (built following Figure 4c) shows M1 as the room temperature ground state across all RE-UT-$VO_2$ thicknesses examined. Stabilizing M1 in a strongly correlated oxide fundamentally expands the accessible electronic phase space, accounting for the observed improvement in the MIT amplitude. Figure 6i compiles recent reports of MIT resistance changes in UT-$VO_2$ categorized by the deposition method. Our remotely epitaxial, magnetron-sputtered UT-$VO_2$ outperforms the vast majority of prior samples, demonstrating a scalable and cost-effective route to high-quality single-crystal UT-$VO_2$ with superior MIT characteristics.

## 4. CONCLUSIONS

In this study, we established an integrated experimental−computational framework to deterministically control the symmetry and transport of ultrathin $VO_2$ on $TiO_2$(001). Direct epitaxy produces rutile pinning in the thinnest limit owing to interfacial clamping, whereas inserting a nanometer-thick amorphous $Al_2O_3$ spacer (remote epitaxy) preserves the epitaxial registry while mitigating clamping, enabling stabilization of the monoclinic M1 phase at room temperature. Through DFT calculations, we confirmed the feasibility of remote epitaxy by demonstrating electric potential transmission through nanometer-thick interlayers and analyzed charge density distributions showing periodic patterns at the $Al_2O_3$ surface. DFT modeling of the V−V bond statistics and dimerization indices revealed the phase evolution from pinned-rutile states to relaxed monoclinic states. High-resolution XRD, Raman, and aberration-corrected STEM collectively map a thickness−strain−temperature phase diagram that resolves a pinned-rutile regime, a coexistence window, and a relaxed monoclinic regime. Geometric phase analysis and XRD revealed that the amorphous $Al_2O_3$ buffer layer reduces interfacial strain from >1.2% to below 0.5%, enabling monoclinic phase stabilization in 20 nm films at room temperature. This strain alleviation dramatically enhanced the MIT properties; the resistivity change across the transition increased from approximately 2500 times in direct epitaxial films to 6500 times in remote epitaxial samples. Crucially, this enhancement was achieved while preserving the relatively low transition temperature characteristic of UT-$VO_2$, maintaining possible device functionality near room temperature. The remote epitaxy approach, which is fully compatible with microelectronics fabrication, provides a robust strain-engineering strategy for optimizing ultrathin $VO_2$ films. This work demonstrates that decoupling the epitaxial registry from mechanical strain through ultrathin buffer layers enables the precise control of phase transitions in strongly correlated oxides for advanced electronic and optoelectronic applications.

## ■ ASSOCIATED CONTENT

### Data Availability Statement

Data will be made available on request.

### Supporting Information

The Supporting Information is available free of charge at https://pubs.acs.org/doi/10.1021/acsami.5c18705.

DFT calculation and molecular dynamics simulations; schematics of direct epitaxy and remote epitaxy samples in this study; supporting optical and spectroscopy (XRD) characterizations of samples in this study; cross-sectional atomic-resolution STEM of interfacial strain; detailed resistivity−temperature plots (PDF)

## ■ AUTHOR INFORMATION


### Corresponding Authors

**Xing Li** − *International Institute for Intelligent Nanorobots and Nanosystems & State Key Laboratory of Surface Physics, College of Intelligent Robotics and Advanced Manufacturing, Fudan University, Shanghai 200438, People's Republic of China; Zhejiang Key Laboratory of Extreme Environment Functional Materials, Yiwu Research Institute of Fudan University, Yiwu 322000, People's Republic of China;* orcid.org/0009-0007-7813-6003; Email: usst_lx@126.com

**Jinshui Miao** − *State Key Laboratory of Infrared Physics, Shanghai Institute of Technical Physics, Chinese Academy of Sciences, Shanghai 200083, People's Republic of China;* orcid.org/0000-0002-0576-5913; Email: jsmiao@mail.sitp.ac.cn

**Yongfeng Mei** − *International Institute for Intelligent Nanorobots and Nanosystems & State Key Laboratory of Surface Physics, College of Intelligent Robotics and Advanced Manufacturing, Fudan University, Shanghai 200438, People's Republic of China; Zhejiang Key Laboratory of Extreme Environment Functional Materials, Yiwu Research Institute of Fudan University, Yiwu 322000, People's Republic of China; Shanghai Frontiers Science Research Base of Intelligent Optoelectronics and Perception, Institute of Optoelectronics, Fudan University, Shanghai 200438, People's Republic of China;* orcid.org/0000-0002-3314-6108; Email: yfm@fudan.edu.cn

### Authors

**Zhi Zheng** − *International Institute for Intelligent Nanorobots and Nanosystems & State Key Laboratory of Surface Physics,*

*College of Intelligent Robotics and Advanced Manufacturing, Fudan University, Shanghai 200438, People's Republic of China; Zhejiang Key Laboratory of Extreme Environment Functional Materials, Yiwu Research Institute of Fudan University, Yiwu 322000, People's Republic of China*

**Xiang Dong** − *International Institute for Intelligent Nanorobots and Nanosystems & State Key Laboratory of Surface Physics, College of Intelligent Robotics and Advanced Manufacturing, Fudan University, Shanghai 200438, People's Republic of China; Zhejiang Key Laboratory of Extreme Environment Functional Materials, Yiwu Research Institute of Fudan University, Yiwu 322000, People's Republic of China*

**Tianjun Cai** − *International Institute for Intelligent Nanorobots and Nanosystems & State Key Laboratory of Surface Physics, College of Intelligent Robotics and Advanced Manufacturing, Fudan University, Shanghai 200438, People's Republic of China; Zhejiang Key Laboratory of Extreme Environment Functional Materials, Yiwu Research Institute of Fudan University, Yiwu 322000, People's Republic of China*

**Yang Wang** − *International Institute for Intelligent Nanorobots and Nanosystems & State Key Laboratory of Surface Physics, College of Intelligent Robotics and Advanced Manufacturing, Fudan University, Shanghai 200438, People's Republic of China; Zhejiang Key Laboratory of Extreme Environment Functional Materials, Yiwu Research Institute of Fudan University, Yiwu 322000, People's Republic of China*

**Binmin Wu** − *State Key Laboratory of Infrared Physics, Shanghai Institute of Technical Physics, Chinese Academy of Sciences, Shanghai 200083, People's Republic of China*

**Ziyu Zhang** − *International Institute for Intelligent Nanorobots and Nanosystems & State Key Laboratory of Surface Physics, College of Intelligent Robotics and Advanced Manufacturing, Fudan University, Shanghai 200438, People's Republic of China; Zhejiang Key Laboratory of Extreme Environment Functional Materials, Yiwu Research Institute of Fudan University, Yiwu 322000, People's Republic of China*

Complete contact information is available at:
https://pubs.acs.org/10.1021/acsami.5c18705

### Author Contributions

Zhi Zeng: conceptualization; investigation; methodology; and writing—original draft; X.L.: conceptualization; supervision; and writing—review and editing. X.D.: investigation. T.C.: methodology. Y.W.: methodology. B.W.: investigation. Ziyu Zhang: investigation. J.M.: funding acquisition; Y.M.: conceptualization; supervision; funding acquisition; and writing—review and editing.

### Funding

This work is supported by the National Natural Science Foundation of China (62375054), the Science and Technology Commission of Shanghai Municipality (24520750200, 24CL2900200), and the Shanghai Talent Programs. This work is supported by the Open Fund of State Key Laboratory of Infrared Physics (Grant No. SITP-NLIST-ZD-2024-04), the CAS Project for Young Scientists in Basic Research (YSBR-113), and the National Natural Science Foundation of China (62334011).

### Notes

The authors declare no competing financial interest.

## REFERENCES

(1) Bauer, E.; Poppa, H. Recent Advances in Epitaxy. *Thin Solid Films* **1972**, *12* (1), 167−185.

(2) Cho, A. Y.; Arthur, J. R. Molecular Beam Epitaxy. *Prog. Solid State Chem.* **1975**, *10*, 157−191.

(3) Chen, Y.; Lei, Y.; Li, Y.; Yu, Y.; Cai, J.; Chiu, M.-H.; Rao, R.; Gu, Y.; Wang, C.; Choi, W.; Hu, H.; Wang, C.; Li, Y.; Song, J.; Zhang, J.; Qi, B.; Lin, M.; Zhang, Z.; Islam, A. E.; Maruyama, B.; Dayeh, S.; Li, L.-J.; Yang, K.; Lo, Y.-H.; Xu, S. Strain Engineering and Epitaxial Stabilization of Halide Perovskites. *Nature* **2020**, *577* (7789), 209−215.

(4) Du, L.; Molas, M. R.; Huang, Z.; Zhang, G.; Wang, F.; Sun, Z. Moiré Photonics and Optoelectronics. *Science* **2023**, *379* (6639), No. eadg0014.

(5) Liu, M. K.; Wagner, M.; Abreu, E.; Kittiwatanakul, S.; McLeod, A.; Fei, Z.; Goldflam, M.; Dai, S.; Fogler, M. M.; Lu, J.; Wolf, S. A.; Averitt, R. D.; Basov, D. N. Anisotropic Electronic State via Spontaneous Phase Separation in Strained Vanadium Dioxide Films. *Phys. Rev. Lett.* **2013**, *111* (9), No. 096602.

(6) Martin, L. W.; Rappe, A. M. Thin-Film Ferroelectric Materials and Their Applications. *Nat. Rev. Mater.* **2017**, *2* (2), 1−14.

(7) Yuan, R.; Duan, Q.; Tiw, P. J.; Li, G.; Xiao, Z.; Jing, Z.; Yang, K.; Liu, C.; Ge, C.; Huang, R.; Yang, Y. A Calibratable Sensory Neuron Based on Epitaxial $VO_2$ for Spike-Based Neuromorphic Multisensory System. *Nat. Commun.* **2022**, *13* (1), No. 3973.

(8) Chen, Y.; Zhang, S.; Ke, F.; Ko, C.; Lee, S.; Liu, K.; Chen, B.; Ager, J. W.; Jeanloz, R.; Eyert, V.; Wu, J. Pressure−Temperature Phase Diagram of Vanadium Dioxide. *Nano Lett.* **2017**, *17* (4), 2512−2516.

(9) Bai, L.; Li, Q.; Corr, S. A.; Meng, Y.; Park, C.; Sinogeikin, S. V.; Ko, C.; Wu, J.; Shen, G. Pressure-Induced Phase Transitions and Metallization in $VO_2$. *Phys. Rev. B* **2015**, *91* (10), No. 104110.

(10) Birkhölzer, Y. A.; Sotthewes, K.; Gauquelin, N.; Riekehr, L.; Jannis, D.; van der Minne, E.; Bu, Y.; Verbeeck, J.; Zandvliet, H. J. W.; Koster, G.; Rijnders, G. High-Strain-Induced Local Modification of the Electronic Properties of $VO_2$ Thin Films. *ACS Appl. Electron. Mater.* **2022**, *4* (12), 6020−6028.

(11) Locquet, J.-P.; Perret, J.; Fompeyrine, J.; Mächler, E.; Seo, J. W.; Van Tendeloo, G. Doubling the Critical Temperature of La1.9Sr0.1CuO4 Using Epitaxial Strain. *Nature* **1998**, *394* (6692), 453−456.

(12) Bozovic, I.; Logvenov, G.; Belca, I.; Narimbetov, B.; Sveklo, I. Epitaxial Strain and Superconductivity in $La_{2-x}Sr_xCuO_4$ Thin Films. *Phys. Rev. Lett.* **2002**, *89* (10), No. 107001.

(13) Diéguez, O.; Rabe, K. M.; Vanderbilt, D. First-Principles Study of Epitaxial Strain in Perovskites. *Phys. Rev. B* **2005**, *72* (14), No. 144101.

(14) Ederer, C.; Spaldin, N. A. Effect of Epitaxial Strain on the Spontaneous Polarization of Thin Film Ferroelectrics. *Phys. Rev. Lett.* **2005**, *95* (25), No. 257601.

(15) Nair, S.; Yang, Z.; Lee, D.; Guo, S.; Sadowski, J. T.; Johnson, S.; Saboor, A.; Li, Y.; Zhou, H.; Comes, R. B.; Jin, W.; Mkhoyan, K. A.; Janotti, A.; Jalan, B. Engineering Metal Oxidation Using Epitaxial Strain. *Nat. Nanotechnol.* **2023**, *18* (9), 1005−1011.

(16) Marcus, P. M. Epitaxial Strain and Epitaxial Bending. *Surf. Sci.* **1996**, *366* (1), 219−227.

(17) Bae, S.-H.; Lu, K.; Han, Y.; Kim, S.; Qiao, K.; Choi, C.; Nie, Y.; Kim, H.; Kum, H. S.; Chen, P.; Kong, W.; Kang, B.-S.; Kim, C.; Lee, J.; Baek, Y.; Shim, J.; Park, J.; Joo, M.; Muller, D. A.; Lee, K.; Kim, J. Graphene-Assisted Spontaneous Relaxation towards Dislocation-Free Heteroepitaxy. *Nat. Nanotechnol.* **2020**, *15* (4), 272−276.

(18) Cao, J.; Ertekin, E.; Srinivasan, V.; Fan, W.; Huang, S.; Zheng, H.; Yim, J. W. L.; Khanal, D. R.; Ogletree, D. F.; Grossman, J. C.; Wu, J. Strain Engineering and One-Dimensional Organization of Metal−Insulator Domains in Single-Crystal Vanadium Dioxide Beams. *Nat. Nanotechnol.* **2009**, *4* (11), 732−737.

(19) Kim, Y.; Cruz, S. S.; Lee, K.; Alawode, B. O.; Choi, C.; Song, Y.; Johnson, J. M.; Heidelberger, C.; Kong, W.; Choi, S.; Qiao, K.; Almansouri, I.; Fitzgerald, E. A.; Kong, J.; Kolpak, A. M.; Hwang, J.;

Kim, J. Remote Epitaxy through Graphene Enables Two-Dimensional Material-Based Layer Transfer. *Nature* **2017**, *544* (7650), 340−343.
(20) Liu, C.; Li, X.; Wang, Y.; Zheng, Z.; Wu, B.; He, W.; Dong, X.; Zhang, Z.; Chen, B.; Huang, J.; An, Z.; Zheng, C.; Huang, G.; Mei, Y. Remote Epitaxy and Exfoliation of Vanadium Dioxide via Sub-Nanometer Thick Amorphous Interlayer. *Nat. Commun.* **2025**, *16* (1), No. 150.
(21) Dou, Z.; Chen, Z.; Li, N.; Yang, S.; Yu, Z.; Sun, Y.; Li, Y.; Liu, B.; Luo, Q.; Ma, T.; Liao, L.; Liu, Z.; Gao, P. Atomic Mechanism of Strong Interactions at the Graphene/Sapphire Interface. *Nat. Commun.* **2019**, *10* (1), No. 5013.
(22) Guo, Y.; Sun, X.; Jiang, J.; Wang, B.; Chen, X.; Yin, X.; Qi, W.; Gao, L.; Zhang, L.; Lu, Z.; Jia, R.; Pendse, S.; Hu, Y.; Chen, Z.; Wertz, E.; Gall, D.; Feng, J.; Lu, T.-M.; Shi, J. A Reconfigurable Remotely Epitaxial $VO_2$ Electrical Heterostructure. *Nano Lett.* **2020**, *20* (1), 33−42.
(23) Liu, B.; Chen, Q.; Chen, Z.; Yang, S.; Shan, J.; Liu, Z.; Yin, Y.; Ren, F.; Zhang, S.; Wang, R.; Wu, M.; Hou, R.; Wei, T.; Wang, J.; Sun, J.; Li, J.; Liu, Z.; Liu, Z.; Gao, P. Atomic Mechanism of Strain Alleviation and Dislocation Reduction in Highly Mismatched Remote Heteroepitaxy Using a Graphene Interlayer. *Nano Lett.* **2022**, *22* (8), 3364−3371.
(24) Okimura, K.; Sakai, J. Changes in Lattice Parameters of $VO_2$ Films Grown on C-Plane Al2O3 Substrates across Metal−Insulator Transition. *Jpn. J. Appl. Phys.* **2009**, *48* (4R), No. 045504.
(25) Mansingh, A.; Singh, R.; Krupanidhi, S. B. Electrical Switching in Single Crystal $VO_2$. *Solid-State Electron.* **1980**, *23* (6), 649−654.
(26) Zhang, H.-T.; Zhang, L.; Mukherjee, D.; Zheng, Y.-X.; Haislmaier, R. C.; Alem, N.; Engel-Herbert, R. Wafer-Scale Growth of $VO_2$ Thin Films Using a Combinatorial Approach. *Nat. Commun.* **2015**, *6* (1), No. 8475.
(27) Choi, H. S.; Ahn, J. S.; Jung, J. H.; Noh, T. W.; Kim, D. H. Mid-Infrared Properties of a $VO_2$ Film near the Metal-Insulator Transition. *Phys. Rev. B* **1996**, *54* (7), 4621−4628.
(28) Wegkamp, D.; Stähler, J. Ultrafast Dynamics during the Photoinduced Phase Transition in $VO_2$. *Prog. Surf. Sci.* **2015**, *90* (4), 464−502.
(29) Shao, Z.; Cao, X.; Luo, H.; Jin, P. Recent Progress in the Phase-Transition Mechanism and Modulation of Vanadium Dioxide Materials. *NPG Asia Mater.* **2018**, *10* (7), 581−605.
(30) Aetukuri, N. B.; Gray, A. X.; Drouard, M.; Cossale, M.; Gao, L.; Reid, A. H.; Kukreja, R.; Ohldag, H.; Jenkins, C. A.; Arenholz, E.; Roche, K. P.; Dürr, H. A.; Samant, M. G.; Parkin, S. S. P. Control of the Metal−Insulator Transition in Vanadium Dioxide by Modifying Orbital Occupancy. *Nat. Phys.* **2013**, *9* (10), 661−666.
(31) Zhi, B.; Gao, G.; Tan, X.; Chen, P.; Wang, L.; Jin, S.; Wu, W. Thickness-Dependent Metal-to-Insulator Transition in Epitaxial $VO_2$ Films. *Mater. Res. Express* **2014**, *1* (4), No. 046402.
(32) Quackenbush, N. F.; Tashman, J. W.; Mundy, J. A.; Sallis, S.; Paik, H.; Misra, R.; Moyer, J. A.; Guo, J.-H.; Fischer, D. A.; Woicik, J. C.; Muller, D. A.; Schlom, D. G.; Piper, L. F. J. Nature of the Metal Insulator Transition in ultra-thin Epitaxial Vanadium Dioxide. *Nano Lett.* **2013**, *13* (10), 4857−4861.
(33) Fan, L. L.; Chen, S.; Luo, Z. L.; Liu, Q. H.; Wu, Y. F.; Song, L.; Ji, D. X.; Wang, P.; Chu, W. S.; Gao, C.; Zou, C. W.; Wu, Z. Y. Strain Dynamics of ultra-thin VO $_2$ Film Grown on $TiO_2$ (001) and the Associated Phase Transition Modulation. *Nano Lett.* **2014**, *14* (7), 4036−4043.
(34) Nagashima, K.; Yanagida, T.; Tanaka, H.; Kawai, T. Stress Relaxation Effect on Transport Properties of Strained Vanadium Dioxide Epitaxial Thin Films. *Phys. Rev. B* **2006**, *74* (17), No. 172106.
(35) Lahneman, D. J.; Slusar, T.; Beringer, D. B.; Jiang, H.; Kim, C.-Y.; Kim, H.-T.; Qazilbash, M. M. Insulator-to-Metal Transition in ultra-thin Rutile $VO_2/TiO_2$(001). *npj Quantum Mater.* **2022**, *7* (1), No. 72.
(36) Lee, D.; Chung, B.; Shi, Y.; Kim, G.-Y.; Campbell, N.; Xue, F.; Song, K.; Choi, S.-Y.; Podkaminer, J. P.; Kim, T. H.; Ryan, P. J.; Kim, J.-W.; Paudel, T. R.; Kang, J.-H.; Spinuzzi, J. W.; Tenne, D. A.; Tsymbal, E. Y.; Rzchowski, M. S.; Chen, L. Q.; Lee, J.; Eom, C. B. Isostructural Metal-Insulator Transition in $VO_2$. *Science* **2018**, *362* (6418), 1037−1040.
(37) Muraoka, Y.; Hiroi, Z. Metal−Insulator Transition of $VO_2$ Thin Films Grown on TiO2 (001) and (110) Substrates. *Appl. Phys. Lett.* **2002**, *80* (4), 583−585.
(38) Hÿtch, M.; Snoeck, E.; Kilaas, R. Quantitative Measurement of Displacement and Strain Fields from HREM Micrographs. *Ultramicroscopy* **1998**, *74* (3), 131−146.
(39) Restori, R.; Schwarzenbach, D.; Schneider, J. R. Charge Density in Rutile, $TiO_2$. *Acta Crystallogr., Sect. B: Struct. Sci.* **1987**, *43* (3), 251−257.
(40) Wang, V.; Xu, N.; Liu, J.-C.; Tang, G.; Geng, W.-T. VASPKIT: A User-Friendly Interface Facilitating High-Throughput Computing and Analysis Using VASP Code. *Comput. Phys. Commun.* **2021**, *267*, No. 108033.
(41) Sandiumenge, F.; Rodríguez, L.; Pruneda, M.; Magén, C.; Santiso, J.; Catalan, G. Metallic Diluted Dimerization in $VO_2$ Tweeds. *Adv. Mater.* **2021**, *33* (9), No. 2004374.
(42) Ahmadi, M.; Atul, A.; de Graaf, S.; van der Veer, E.; Meise, A.; Tavabi, A. H.; Heggen, M.; Dunin-Borkowski, R. E.; Ahmadi, M.; Kooi, B. J. Atomically Resolved Phase Coexistence in $VO_2$ Thin Films. *ACS Nano* **2024**, *18* (21), 13496−13505.
(43) Gražulis, S.; Chateigner, D.; Downs, R. T.; Yokochi, A. F. T.; Quirós, M.; Lutterotti, L.; Manakova, E.; Butkus, J.; Moeck, P.; Le Bail, A. Crystallography Open Database—an Open-Access Collection of Crystal Structures. *J. Appl. Crystallogr.* **2009**, *42* (4), 726−729.
(44) Jain, A.; Ong, S. P.; Hautier, G.; Chen, W.; Richards, W. D.; Dacek, S.; Cholia, S.; Gunter, D.; Skinner, D.; Ceder, G.; Persson, K. A. Commentary: The Materials Project: A Materials Genome Approach to Accelerating Materials Innovation. *APL Mater.* **2013**, *1* (1), No. 011002.
(45) Fitting, L.; Thiel, S.; Schmehl, A.; Mannhart, J.; Muller, D. A. Subtleties in ADF Imaging and Spatially Resolved EELS: A Case Study of Low-Angle Twist Boundaries in SrTiO3. *Ultramicroscopy* **2006**, *106* (11), 1053−1061.
(46) Yu, Z.; Muller, D. A.; Silcox, J. Effects of Specimen Tilt in ADF-STEM Imaging of a-Si/c-Si Interfaces. *Ultramicroscopy* **2008**, *108* (5), 494−501.
(47) Schilbe, P. Raman Scattering in $VO_2$. *Phys. B* **2002**, *316*−*317*, 600−602.
(48) Mondal, W. R.; Evlyukhin, E.; Howard, S. A.; Paez, G. J.; Paik, H.; Schlom, D. G.; Piper, L. F. J.; Lee, W.-C. Role of V-V Dimers on Structural, Electronic, Magnetic, and Vibrational Properties of $VO_2$ by First-Principles Simulations and Raman Spectroscopic Analysis. *Phys. Rev. B* **2021**, *103* (21), No. 214107.
(49) Fultz, B.; Howe, J. M. *Transmission Electron Microscopy and Diffractometry of Materials*; Springer Science & Business Media, 2012.
(50) Treacy, M. M. J.; Gibson, J. M.; Short, K. T.; Rice, S. B. Channeling Effects from Impurity Atoms in the High-Angle Annular Detector of the Stem. *Ultramicroscopy* **1988**, *26* (1), 133−142.
(51) Lakner, H.; Bollig, B.; Ungerechts, S.; Kubalek, E. Characterization of III - V Semiconductor Interfaces by Z-Contrast Imaging, EELS and CBED. *J. Phys. D: Appl. Phys.* **1996**, *29* (7), 1767.
(52) Preziosi, D.; Lopez-Mir, L.; Li, X.; Cornelissen, T.; Lee, J. H.; Trier, F.; Bouzehouane, K.; Valencia, S.; Gloter, A.; Barthélémy, A.; Bibes, M. Direct Mapping of Phase Separation across the Metal−Insulator Transition of $NdNiO_3$. *Nano Lett.* **2018**, *18* (4), 2226−2232.
(53) Yang, Y.; Mao, X.; Yao, Y.; Huang, H.; Lu, Y.; Luo, L.; Zhang, X.; Yin, G.; Yang, T.; Gao, X. Thickness Effects on the Epitaxial Strain States and Phase Transformations in (001)-$VO_2/TiO_2$ Thin Films. *J. Appl. Phys.* **2019**, *125* (8), No. 082508.
(54) Hong, B.; Yang, Y.; Hu, K.; Dong, Y.; Zhou, J.; Zhang, Y.; Zhao, W.; Luo, Z.; Gao, C. Strain Engineering on the Metal-Insulator Transition of $VO_2/TiO_2$ Epitaxial Films Dependent on the Strain State of Vanadium Dimers. *Appl. Phys. Lett.* **2019**, *115* (25), No. 251605.
(55) Lee, D. K.; Park, Y.; Sim, H.; Park, J.; Kim, Y.; Kim, G.-Y.; Eom, C.-B.; Choi, S.-Y.; Son, J. Heterogeneous Integration of Single-

Crystalline Rutile Nanomembranes with Steep Phase Transition on Silicon Substrates. *Nat. Commun.* **2021**, *12* (1), No. 5019.
(56) Cui, Y.; Ramanathan, S. Substrate Effects on Metal-Insulator Transition Characteristics of Rf-Sputtered Epitaxial $VO_2$ Thin Films. *J. Vac. Sci. Technol., A* **2011**, *29* (4), No. 041502.
(57) Yang, M.; Yang, Y.; Hong, B.; Wang, L.; Hu, K.; Dong, Y.; Xu, H.; Huang, H.; Zhao, J.; Chen, H.; Song, L.; Ju, H.; Zhu, J.; Bao, J.; Li, X.; Gu, Y.; Yang, T.; Gao, X.; Luo, Z.; Gao, C. Suppression of Structural Phase Transition in $VO_2$ by Epitaxial Strain in Vicinity of Metal-Insulator Transition. *Sci. Rep.* **2016**, *6* (1), No. 23119.
(58) Paik, H.; Moyer, J. A.; Spila, T.; Tashman, J. W.; Mundy, J. A.; Freeman, E.; Shukla, N.; Lapano, J. M.; Engel-Herbert, R.; Zander, W.; Schubert, J.; Muller, D. A.; Datta, S.; Schiffer, P.; Schlom, D. G. Transport Properties of Ultra-Thin $VO_2$ Films on (001) $TiO_2$ Grown by Reactive Molecular-Beam Epitaxy. *Appl. Phys. Lett.* **2015**, *107* (16), No. 163101.
(59) Kim, H. K.; You, H.; Chiarello, R. P.; Chang, H. L. M.; Zhang, T. J.; Lam, D. J. Finite-Size Effect on the First-Order Metal-Insulator Transition in $VO_2$ Films Grown by Metal-Organic Chemical-Vapor Deposition. *Phys. Rev. B* **1993**, *47* (19), 12900−12907.
(60) Kim, H.; Chang, C. S.; Lee, S.; Jiang, J.; Jeong, J.; Park, M.; Meng, Y.; Ji, J.; Kwon, Y.; Sun, X.; Kong, W.; Kum, H. S.; Bae, S.-H.; Lee, K.; Hong, Y. J.; Shi, J.; Kim, J. Remote Epitaxy. *Nat. Rev. Methods Primers* **2022**, *2* (1), No. 40.
(61) Chang, C. S.; Kim, K. S.; Park, B.-I.; Choi, J.; Kim, H.; Jeong, J.; Barone, M.; Parker, N.; Lee, S.; Zhang, X.; Lu, K.; Suh, J. M.; Kim, J.; Lee, D.; Han, N. M.; Moon, M.; Lee, Y. S.; Kim, D.-H.; Schlom, D. G.; Hong, Y. J.; Kim, J. Remote Epitaxial Interaction through Graphene. *Sci. Adv.* **2023**, *9* (42), No. eadj5379.

https://doi.org/10.1021/acsami.5c18705
ACS Appl. Mater. Interfaces 2025, 17, 70203−70216